Supporting Information

Dynamics of frequency-swept nuclear spin optical pumping in powdered diamond at low magnetic fields

Pablo R. Zangara[1], Siddharth Dhomkar[1], Ashok Ajoy[3], Kristina Liu[3], Raffi Nazaryan[3], Daniela Pagliero[1], Dieter Suter[5], Jeffrey A. Reimer[4], Alexander Pines[3], Carlos A. Meriles[1,2]

[1]Dept. of Physics, CUNY-City College of New York, New York, NY 10031, USA.
[2]CUNY-Graduate Center, New York, NY 10016, USA.
[3]Department of Chemistry, University of California Berkeley, and Materials Science Division Lawrence Berkeley National Laboratory, Berkeley, California 94720, USA.
[4]Department of Chemical and Biomolecular Engineering, and Materials Science Division Lawrence Berkeley National Laboratory University of California, Berkeley, California 94720, USA.
[5]Fakultät Physik, Technische Universität Dortmund, D-44221 Dortmund, Germany.

I. The effective secular approximation

Here we show how to derive Eq. (4) of the main text from the application of average Hamiltonian theory (AHT) to Eq. (1), using the energy constrains in Eq. (2). We start by writing the Hamiltonian in Eq. (1) as

$$H = \Delta((\mathrm{S^z})^2 - \mathrm{S}(\mathrm{S}+1)/3) - \gamma_\mathrm{e}\left(B_\mathrm{x}\mathrm{S^x} + B_\mathrm{y}\mathrm{S^y} + B_\mathrm{z}\mathrm{S^z}\right) - \gamma_\mathrm{C}\mathbf{B}\cdot\mathbf{I} + A_{\mathrm{xx}}\mathrm{S^x}\mathrm{I^x} + A_{\mathrm{yy}}\mathrm{S^y}\mathrm{I^y} + A_{\mathrm{zz}}\mathrm{S^z}\mathrm{I^z} + A_{\mathrm{zx}}(\mathrm{S^x}\mathrm{I^z} + \mathrm{S^z}\mathrm{I^x})\,. \quad \text{(A.1)}$$

Following the standard AHT recipe (1,2), we split (A.1) into two parts, $H = H_\Delta + H_1$, where $H_\Delta = \Delta((\mathrm{S^z})^2 - \mathrm{S}(\mathrm{S}+1)/3)$ encloses the highest energy scale (or, equivalently, provides for the fastest dynamics), and H_1 is automatically defined as $H - H_\Delta$. The zeroth order in AHT is given by

$$\overline{H}^{(0)} = \frac{1}{T_\Delta}\int_0^{T_\Delta} U_\Delta^\dagger(t')\mathrm{H}_1 U_\Delta\ (t')dt'\,, \quad \text{(A.2)}$$

where $T_\Delta = 2\pi/\Delta$ and $U_\Delta\ (t) = exp\left\{-\frac{i}{\hbar}H_\Delta t\right\}$. It is useful to define $\mathcal{H}_1(\mathrm{t}) = U_\Delta^\dagger(t)\mathrm{H}_1 U_\Delta\ (t)$, which we rewrite as,

$$\mathcal{H}_1(\mathrm{t}) = -\gamma_\mathrm{e}\left(B_\mathrm{x}\mathrm{S_t^x} + B_\mathrm{y}\mathrm{S_t^y}(\mathrm{t}) + B_\mathrm{z}\mathrm{S^z}\right) - \gamma_\mathrm{C}\mathbf{B}\cdot\mathbf{I} + A_{\mathrm{xx}}\mathrm{S_t^x}\mathrm{I^x} + A_{\mathrm{yy}}\mathrm{S_t^y}\mathrm{I^y} + A_{\mathrm{zz}}\mathrm{S^z}\mathrm{I^z} + A_{zx}(\mathrm{S_t^x}\mathrm{I^z} + \mathrm{S^z}\mathrm{I^x})\,, \quad \text{(A.3)}$$

where

$$\mathrm{S_t^x} = U_\Delta^\dagger(t)\mathrm{S^x}U_\Delta\ (t) = \frac{\sqrt{2}}{2}\begin{bmatrix} 0 & exp\left\{\frac{i}{\hbar}\Delta t\right\} & 0 \\ exp\left\{-\frac{i}{\hbar}\Delta t\right\} & 0 & exp\left\{-\frac{i}{\hbar}\Delta t\right\} \\ 0 & exp\left\{\frac{i}{\hbar}\Delta t\right\} & 0 \end{bmatrix}, \quad \text{(A.4)}$$

$$\mathrm{S_t^y} = U_\Delta^\dagger(t)\mathrm{S}^y U_\Delta\ (t) = \frac{\sqrt{2}i}{2}\begin{bmatrix} 0 & -exp\left\{\frac{i}{\hbar}\Delta t\right\} & 0 \\ exp\left\{-\frac{i}{\hbar}\Delta t\right\} & 0 & -exp\left\{-\frac{i}{\hbar}\Delta t\right\} \\ 0 & exp\left\{\frac{i}{\hbar}\Delta t\right\} & 0 \end{bmatrix}. \quad \text{(A.5)}$$

www.pnas.org/cgi/doi/10.1073/pnas.1811994116

Upon integrating, it is straightforward to show that

$$\overline{H}^{(0)} = -\gamma_e B_z S^z - \gamma_C \mathbf{B}\cdot\mathbf{I} + A_{zz} S^z I^z + A_{zx} S^z I^x, \tag{A.6}$$

which is, in fact, a valid secular approximation in the aligned case ($\theta = 0$).

The following order in AHT is given by

$$\overline{H}^{(1)} = \frac{-i}{2T_\Delta}\int_0^{T_\Delta} dt_1 \int_0^{t_1} dt_2 [\mathcal{H}_1(t_1), \mathcal{H}_1(t_2)]\,. \tag{A.7}$$

In what follows, we disregard any term in the previous commutator involving $-\gamma_C \mathbf{B}\cdot\mathbf{I}$ since it produces negligible contributions. Any term in the commutator $[\mathcal{H}_1(t_1), \mathcal{H}_1(t_2)]$ would then be of the form $[S^z, S_t^\alpha]$ or $\left[S_t^\alpha, S_{t'}^{\alpha'}\right]$, where $\alpha, \alpha' \in \{x, y\}$ and $t, t' \in \{t_1, t_2\}$. Let us start by considering the terms of the form $[S^z, S_t^\alpha]$:

$$[S^z, S_t^x] = iS_t^y\,, \tag{A.8}$$

$$\left[S^z, S_t^y\right] = -iS_t^x\,. \tag{A.9}$$

Then,

$$\frac{-i}{2T_\Delta}\int_0^{T_\Delta} dt_1 \int_0^{t_1} dt_2 S_{t_2}^x = \frac{\sqrt{2}}{4\Delta}\begin{bmatrix} 0 & 1 & 0 \\ -1 & 0 & -1 \\ 0 & 1 & 0 \end{bmatrix}, \tag{A.10}$$

$$\frac{-i}{2T_\Delta}\int_0^{T_\Delta} dt_1 \int_0^{t_1} dt_2 S_{t_2}^y = \frac{\sqrt{2}i}{4\Delta}\begin{bmatrix} 0 & -1 & 0 \\ -1 & 0 & 1 \\ 0 & 1 & 0 \end{bmatrix}, \tag{A.11}$$

$$\frac{-i}{2T_\Delta}\int_0^{T_\Delta} dt_1 \int_0^{t_1} dt_2 S_{t_1}^x = \frac{\sqrt{2}}{4\Delta}\begin{bmatrix} 0 & -1 & 0 \\ 1 & 0 & 1 \\ 0 & -1 & 0 \end{bmatrix}, \tag{A.12}$$

$$\frac{-i}{2T_\Delta}\int_0^{T_\Delta} dt_1 \int_0^{t_1} dt_2 S_{t_1}^y = \frac{\sqrt{2}i}{4\Delta}\begin{bmatrix} 0 & 1 & 0 \\ 1 & 0 & -1 \\ 0 & -1 & 0 \end{bmatrix}. \tag{A.13}$$

These terms induce transitions between the subspace $m_S = 0$ and the subspaces $m_S = \pm 1$. The matrix element for these transitions scale as $(\gamma_e B)^2/\Delta \sim 30\text{MHz} \ll \Delta$ so, they are suppressed by the zero-field splitting induced by the crystalline field and we can safely neglect them.

Let us consider the terms $\left[S_t^\alpha, S_{t'}^{\alpha'}\right]$ with $\alpha \neq \alpha'$. After some algebra,

$$\frac{-i}{2T_\Delta}\int_0^{T_\Delta} dt_1 \int_0^{t_1} dt_2 \left[S_{t_1}^x, S_{t_2}^y\right] = \frac{i}{2\Delta}\begin{bmatrix} 0 & 0 & -1 \\ 0 & 0 & 0 \\ 1 & 0 & 0 \end{bmatrix}, \tag{A.14}$$

$$\frac{-i}{2T_\Delta}\int_0^{T_\Delta} dt_1 \int_0^{t_1} dt_2 \left[S_{t_1}^y, S_{t_2}^x\right] = \frac{i}{2\Delta}\begin{bmatrix} 0 & 0 & -1 \\ 0 & 0 & 0 \\ 1 & 0 & 0 \end{bmatrix}. \tag{A.15}$$

These contributions induce transitions between the subspaces $m_S = +1$ and $m_S = -1$, with a matrix element scaling, at best, as $(\gamma_e B)^2/\Delta \sim 30\text{MHz} < \gamma_e B$. Thus, even if not as strong as before, there is a truncation of at least one order of magnitude due to the electron Zeeman splitting. We therefore disregard these terms.

Finally, we consider the terms $\left[\mathrm{S}_t^\alpha, \mathrm{S}_{t'}^\alpha\right]$:

$$\frac{-i}{2T_\Delta}\int_0^{T_\Delta} dt_1 \int_0^{t_1} dt_2 \left[\mathrm{S}_{t_1}^{\mathrm{x}}, \mathrm{S}_{t_2}^{\mathrm{x}}\right] = \frac{1}{2\Delta}\begin{bmatrix} 1 & 0 & 1 \\ 0 & -2 & 0 \\ 1 & 0 & 1 \end{bmatrix}, \tag{A.16}$$

$$\frac{-i}{2T_\Delta}\int_0^{T_\Delta} dt_1 \int_0^{t_1} dt_2 \left[\mathrm{S}_{t_1}^{\mathrm{y}}, \mathrm{S}_{t_2}^{\mathrm{y}}\right] = \frac{1}{2\Delta}\begin{bmatrix} 1 & 0 & -1 \\ 0 & -2 & 0 \\ -1 & 0 & 1 \end{bmatrix}. \tag{A.17}$$

By the same criteria, the off-diagonal elements have to be disregarded as they represent transitions between the subspaces $m_\mathrm{S} = +1$ and $m_\mathrm{S} = -1$, which are truncated by the Zeeman splitting. However, the diagonal matrix elements are in fact relevant, since they can induce transitions between different ^{13}C spin states.

Now we insert Eq. (A.3) into Eq. (A.7) and trace the origin of the commutators $\left[\mathrm{S}_t^\alpha, \mathrm{S}_{t'}^\alpha\right]$. These can arise either from terms like $-(\gamma_\mathrm{e} B_\alpha)^2\left[\mathrm{S}_{t_1}^\alpha, \mathrm{S}_{t_2}^\alpha\right]$ or terms like $-\gamma_\mathrm{e} B_\alpha A_{\alpha\alpha}\mathrm{I}^\alpha\left[\mathrm{S}_{t_1}^\alpha, \mathrm{S}_{t_2}^\alpha\right]$. In the first case, the diagonal matrix elements in Eqs. (A.16) and (A.17) produce energy shifts two orders of magnitude smaller than the actual gap $\sim\Delta$ and can be ignored. The second case stands for actual coupling terms between the ^{13}C spin states. These terms have matrix elements as large as $\delta\sim\gamma_e B_\alpha A_{\alpha\alpha}/\Delta\sim 1\times 10^{-1}$MHz for $A_{\alpha\alpha}\sim$1MHz, and up to $\delta\sim$1MHz for $A_{\alpha\alpha}\sim$10MHz. Thus, these transitions are critical for the $m_\mathrm{S} = 0$ subspace, where the Zeeman splitting $-\gamma_\mathrm{C} B$ is no longer the dominant energy scale.

We are left with the following second-order AHT correction according:

$$\overline{H}^{(1)} = \frac{-\gamma_\mathrm{e}}{\Delta}\left[B_\mathrm{x}(A_{\mathrm{xx}}\mathrm{I}^\mathrm{x} + A_{\mathrm{zx}}\mathrm{I}^\mathrm{z}) + B_\mathrm{y} A_{\mathrm{yy}}\mathrm{I}^\mathrm{y}\right]\begin{bmatrix} 1 & 0 & 0 \\ 0 & -2 & 0 \\ 0 & 0 & 1 \end{bmatrix}. \tag{A.18}$$

This Hamiltonian represents a secularization of terms not included in $\overline{H}^{(0)}$, and ultimately leads to the desired secular Hamiltonian, i.e. Eq. (3) in main text, $H_{\mathrm{sec}} = H_\Delta + \overline{H}^{(0)} + \overline{H}^{(1)}$. The effective Hamiltonian introduced in Eq. (4) of the main text follows from a rotating frame transformation,

$$H_{\mathrm{eff}} = H_{\mathrm{sec}} - \omega(\mathrm{S}^\mathrm{z})^2 + \Omega\mathrm{S}^\mathrm{x}, \tag{A.19}$$

where Ω is the Rabi frequency. Note that the term proportional to $(\mathrm{S}^\mathrm{z})^2$ — valid only in the limit $\gamma_\mathrm{e} B < \Delta$ considered herein — simultaneously takes into account contributions from the rotating and counter-rotating terms stemming from the linearly polarized MW field; depending on the value of ω, one or the other becomes resonant across the set of transitions ($m_\mathrm{S} = 0 \leftrightarrow m_\mathrm{S} = -1$) and ($m_\mathrm{S} = 0 \leftrightarrow m_\mathrm{S} = +1$). To simplify the notation, we set $\hbar = 1$ throughout our calculations.

II. Eigenstates and observables

In Fig. S1 we compare the first four eigenstates $|0,\alpha_\uparrow\rangle$, $|0,\alpha_\downarrow\rangle$, $|-1,\beta_\uparrow\rangle$, and $|-1,\beta_\downarrow\rangle$ obtained from the exact Hamiltonian (A.1) and the secular approximation H_{sec} (we omit an equivalent analysis for the subspace $m_s = +1$). The comparison is based on the decomposition of each eigenstate in terms of the computational basis $\{|m_\mathrm{S}, m_\mathrm{I}\rangle\}$ as a function of the angle θ (fixed $\phi = 0$). It is worth noting that the states $|0,\alpha_\uparrow\rangle$ and $|0,\alpha_\downarrow\rangle$ remain predominantly given by $|0,\uparrow\rangle$ and $|0,\downarrow\rangle$ respectively in the range $0° \le \theta \le 90°$. This is also true (and even more accurately so) for $|-1,\beta_\uparrow\rangle$, and $|-1,\beta_\downarrow\rangle$,

which are essentially given by $|-1,\uparrow\rangle$ and $|-1,\downarrow\rangle$ respectively. The inversion observed at 90° simply corresponds to the change in the preferred direction of quantization $z \to -z$.

As discussed in the main text, the LZ crossings create population imbalances between these states, leading to the observed ^{13}C polarization. However, even though the whole process takes place at low magnetic field and in presence of light, the actual signal acquisition throughout our experiments is performed by shuttling the sample into a high-field NMR system. Since such a transfer is intrinsically adiabatic, the population imbalance created at low-field remains unchanged in the high-field condition. This suggests a way to define the ^{13}C polarization in our simulations by algebraically adding the populations in the instantaneous eigen-basis with the sign given by the character of the state (up or down). Alternatively, one can compute the expectation value of the I_z operator rotated in the direction of the magnetic field. In this case, however, the time-dependence of the ^{13}C polarization exhibits fast coherent oscillations which unnecessarily complicate the numerics. Nevertheless, it is important to stress that both ways of computing the ^{13}C polarization give essentially the same results, and that both are in agreement with our experimental observations.

We now turn our attention to estimating the energy gaps δE_{13} and δE_{23} presented in Fig. 1B and the LZ probabilities $p(1|3)$ and $p(2|3)$. We start by assuming the effective Hamiltonian in the aligned case $\theta = 0$, $\phi = 0$,

$$H_{eff}^{[\theta=0,\phi=0]} = \Delta(\mathrm{S^z})^2 - \gamma_e B_z \mathrm{S^z} - \gamma_C B_z \mathrm{I^z} + A_{zz}\mathrm{S^z I^z} + A_{zx}\mathrm{S^z I^x} - \omega(\mathrm{S^z})^2 + \Omega \mathrm{S^x}. \tag{A.20}$$

In what follows, we consider the Hilbert subspace spanned by the basis states $\{|0,\uparrow\rangle, |0,\downarrow\rangle, |-1,\uparrow\rangle, |-1,\downarrow\rangle\}$. By introducing the notation $\omega_{0S} = \Delta - |\gamma_e| B_z$ and $\omega_{0I} = \gamma_C B_z$, the matrix representation of $H_{eff}^{[\theta=0,\phi=0]}$ in this subspace is:

$$H_{eff}^{[\theta=0,\phi=0]} = \begin{array}{c|cccc} & |0,\uparrow\rangle & |0,\downarrow\rangle & |-1,\uparrow\rangle & |-1,\downarrow\rangle \\ \hline \langle 0,\uparrow| & \frac{-\omega_{0I}}{2} & 0 & \frac{\Omega}{2} & 0 \\ \langle 0,\downarrow| & 0 & \frac{\omega_{0I}}{2} & 0 & \frac{\Omega}{2} \\ \langle -1,\uparrow| & \frac{\Omega}{2} & 0 & \omega_{0S} - \frac{\omega_{0I}}{2} - \omega - \frac{A_{zz}}{2} & -\frac{A_{zx}}{2} \\ \langle -1,\downarrow| & 0 & \frac{\Omega}{2} & -\frac{A_{zx}}{2} & \omega_{0S} + \frac{\omega_{0I}}{2} - \omega + \frac{A_{zz}}{2} \end{array} . \tag{A.21}$$

If the MW irradiation is close to the $|0,\downarrow\rangle \leftrightarrow |-1,\uparrow\rangle$ resonance then the two states are degenerate, which means that

$$\omega_{0S} - \frac{\omega_{0I}}{2} - \omega - \frac{A_{zz}}{2} \approx \frac{\omega_{0I}}{2}, \tag{A.22}$$

or, equivalently,

$$\omega_{0S} - \omega_{0I} - \frac{A_{zz}}{2} \approx \omega. \tag{A.23}$$

We therefore rewrite the Hamiltonian as

$$H_{eff}^{[\theta=0,\phi=0]} = \begin{array}{c} \\ \langle 0,\uparrow| \\ \langle 0,\downarrow| \\ \langle -1,\uparrow| \\ \langle -1,\downarrow| \end{array} \begin{array}{cccc} |0,\uparrow\rangle & |0,\downarrow\rangle & |-1,\uparrow\rangle & |-1,\downarrow\rangle \\ \frac{-\omega_{0I}}{2} & 0 & \frac{\Omega}{2} & 0 \\ 0 & \frac{\omega_{0I}}{2} & 0 & \frac{\Omega}{2} \\ \frac{\Omega}{2} & 0 & \frac{\omega_{0I}}{2} & -\frac{A_{zx}}{2} \\ 0 & \frac{\Omega}{2} & -\frac{A_{zx}}{2} & \frac{3}{2}\omega_{0I} + A_{zz} \end{array} . \quad \text{(A.24)}$$

The interaction matrix element $\langle 0,\uparrow|H_{eff}^{[\theta=0,\phi=0]}|-1,\uparrow\rangle = \Omega/2$ corresponds to the NV spin flip produced by the Rabi oscillation. As expected, this corresponds to having $\delta E_{13} \sim \Omega$, and accordingly $p(1|3) \sim exp\left\{-2\pi\,\Omega^2/\dot{\nu}_{MW}\right\}$. The origin of the gap δE_{23} is subtler, and in order to provide for an estimate, we first assume $\omega_{0I} \ll A_{zz}$ and focus on the subspace spanned by the states $\{|0,\uparrow\rangle, |0,\downarrow\rangle, |-1,\uparrow\rangle\}$. We incorporate then energy shifts based on second order perturbation theory,

$$H_{eff,reduced}^{[\theta=0,\phi=0]} = \begin{array}{c} \\ \langle 0,\uparrow| \\ \langle 0,\downarrow| \\ \langle -1,\uparrow| \end{array} \begin{array}{ccc} |0,\uparrow\rangle & |0,\downarrow\rangle & |-1,\uparrow\rangle \\ \frac{-\omega_{0I}}{2} & 0 & \frac{\Omega}{2} \\ 0 & \frac{\omega_{0I}}{2} - \frac{\Omega^2}{4(\omega_{0I}+A_{zz})} & 0 \\ \frac{\Omega}{2} & 0 & \frac{\omega_{0I}}{2} - \frac{A_{zx}^2}{4(\omega_{0I}+A_{zz})} \end{array} . \quad \text{(A.25)}$$

A fairly good approximation for the gap δE_{23} (see below for a comparison with the fully numerical solution) can be obtained by diagonalization,

$$\delta E_{23} \approx \left| \frac{\omega_{0I}}{2} + \frac{\left(A_{zx}^2 - 2\Omega^2\right)}{8(\omega_{0I}+A_{zz})} - \frac{1}{2}\sqrt{\left(\omega_{0I} - \frac{A_{zx}^2}{4(\omega_{0I}+A_{zz})}\right)^2 + \Omega^2} \right| \quad \text{(A.26)}$$

Notice, however, that this estimate is nonzero even if $A_{zx} = 0$. This happens because the degeneracy of the states $|0,\downarrow\rangle$ and $|-1,\uparrow\rangle$ (the condition stated in Eq. (A.22)) is broken by the presence of interaction terms with the states $|0,\uparrow\rangle$ and $|-1,\downarrow\rangle$. These interaction terms do contribute to δE_{23}, but since they are not genuine interaction matrix elements between the states $|0,\downarrow\rangle$ and $|-1,\uparrow\rangle$, they cannot be used to compute the LZ transition probabilities. In other words, the gap δE_{23} is not the actual magnitude ruling the LZ process.

The only way to produce a transition between the states $|0,\downarrow\rangle$ and $|-1,\uparrow\rangle$ would be a second order interaction term between them mediated by the intermediate state $|-1,\downarrow\rangle$. The corresponding matrix element for such a virtual interaction (not present in Eq. (A.25)) is given by

$$J_{virtual} = \frac{\langle 0,\downarrow|H_{eff}^{[\theta=0,\phi=0]}|-1,\downarrow\rangle\langle -1,\downarrow|H_{eff}^{[\theta=0,\phi=0]}|-1,\uparrow\rangle}{\frac{\omega_{0I}}{2} - \langle -1,\downarrow|H_{eff}^{[\theta=0,\phi=0]}|-1,\downarrow\rangle}$$

$$J_{virtual} = \frac{-\Omega A_{zx}}{4\left(\frac{1}{2}\omega_{0I} - \frac{3}{2}\omega_{0I} - A_{zz}\right)} = \frac{\Omega A_{zx}}{4(\omega_{0I}+A_{zz})}. \quad \text{(A.27)}$$

This provides for a fair estimate of the LZ transition probability at the energy crossing between the branches of states $|0,\downarrow\rangle$ and $|-1,\uparrow\rangle$,

$$p(2|3) \sim \exp\left\{-2\pi\left(\frac{\Omega A_{zx}}{4(\omega_{0I}+A_{zz})}\right)^2/\dot{\nu}_{MW}\right\}. \quad \text{(A.28)}$$

Similar arguments can be used for the resonance $|0,\uparrow\rangle \leftrightarrow |-1,\downarrow\rangle$, obtaining the same estimates.

The general case, i.e. arbitrary (θ,ϕ), is more involved. Considering the same 4-state subspace as above, we have

$$H_{eff} = \begin{array}{c|cccc} & |0,\uparrow\rangle & |0,\downarrow\rangle & |-1,\uparrow\rangle & |-1,\downarrow\rangle \\ \langle 0,\uparrow| & \frac{-\omega_{0I}}{2}+F & G & \frac{\Omega}{2} & 0 \\ \langle 0,\downarrow| & G^{\dagger} & \frac{\omega_{0I}}{2}-F & 0 & \frac{\Omega}{2} \\ \langle -1,\uparrow| & \frac{\Omega}{2} & 0 & \omega_{0S}-\frac{\omega_{0I}}{2}-\omega-\frac{A_{zz}}{2}-\frac{F}{2} & -\left(\frac{G+A_{zx}}{2}\right) \\ \langle -1,\downarrow| & 0 & \frac{\Omega}{2} & \left(\frac{G^{\dagger}+A_{zx}}{2}\right) & \omega_{0S}+\frac{\omega_{0I}}{2}-\omega+\frac{A_{zz}}{2}+\frac{F}{2} \end{array} , \quad (A.29)$$

where $F=(\gamma_e/\Delta)B_x A_{zx}$, $G=(\gamma_e/\Delta)\times\left(B_x A_{xx}-iB_y A_{yy}\right)$, and we are neglecting the mixing created by the terms $-\gamma_C B_x I^x - \gamma_C B_y I^y$. As before, we first assume the MW frequency is in near resonance with the $|0,\downarrow\rangle \leftrightarrow |-1,\uparrow\rangle$ transition, meaning that

$$\omega_{0S}-\frac{\omega_{0I}}{2}-\omega-\frac{A_{zz}}{2}-\frac{F}{2}\approx\frac{\omega_{0I}}{2}-F\ , \quad (A.30)$$

or, equivalently,

$$\omega_{0S}-\omega_{0I}-\frac{A_{zz}}{2}+\frac{F}{2}\approx\omega. \quad (A.31)$$

Then,

$$H_{eff} = \begin{array}{c|cccc} & |0,\uparrow\rangle & |0,\downarrow\rangle & |-1,\uparrow\rangle & |-1,\downarrow\rangle \\ \langle 0,\uparrow| & \frac{-\omega_{0I}}{2}+F & G & \frac{\Omega}{2} & 0 \\ \langle 0,\downarrow| & G^{\dagger} & \frac{\omega_{0I}}{2}-F & 0 & \frac{\Omega}{2} \\ \langle -1,\uparrow| & \frac{\Omega}{2} & 0 & \frac{\omega_{0I}}{2}-F & -\left(\frac{G+A_{zx}}{2}\right) \\ \langle -1,\downarrow| & 0 & \frac{\Omega}{2} & -\left(\frac{G^{\dagger}+A_{zx}}{2}\right) & \frac{3\omega_{0I}}{2}+A_{zz} \end{array} . \quad (A.32)$$

Note that while the direct matrix element $\langle 0,\uparrow|H_{eff}|-1,\uparrow\rangle=\Omega/2$ still provides for the estimate $\delta E_{13}\sim\ \Omega$ and $p(1|3)\sim\exp\left\{-2\pi\,\Omega^2/\dot{\nu}_{MW}\right\}$ remains valid, it is not straightforward to calculate or estimate δE_{23}. Regardless, we show in Fig. S2 that the estimate for the aligned case (Eq. (A.26)) is still a fair estimate of δE_{23} for a large range of values of θ.

As before, we are interested in an interaction matrix element between the states $|0,\downarrow\rangle$ and $|-1,\uparrow\rangle$. Again, this is given by a second order interaction term mediated by the intermediate state $|-1,\downarrow\rangle$. Thus, the estimate for the LZ transition probability is in this case

$$p(2|3)\sim\exp\left\{-2\pi\left(\frac{\Omega(G+A_{zx})}{4(\omega_{0I}+A_{zz}+F)}\right)^2/\dot{\nu}_{\mathrm{MW}}\right\}. \quad (A.33)$$

Notice that this estimate reduces to Eq. (A.28) in the limit $(\gamma_e B/\Delta)\to 0$.

The results above provide a simple framework to describe the generation of ^{13}C polarization as a function of the sweep velocity. Indeed, a crude approximation for the nuclear spin polarization can be written as the product $g(\dot{\nu}_{\mathrm{MW}})\times q(\dot{\nu}_{\mathrm{MW}})\times(1-Q(\dot{\nu}_{\mathrm{MW}}))$, where we introduced the notation $Q(\dot{\nu}_{\mathrm{MW}})=p(1|3)$. The last factor $(1-Q(\dot{\nu}_{\mathrm{MW}}))$ measures the adiabaticity during the sweep for branch 1. At low-intermediate velocities (where $Q(\dot{\nu}_{MW})\sim 0$), the factor $q(\dot{\nu}_{\mathrm{MW}})$ equals the

bifurcation probability $p(2|3)$. In the limit of fast sweeps, however, one has to correct $p(2|3)$ with an extra factor $(1 - Q(\dot{\nu}_{\mathrm{MW}})$ that accounts for the transition from branch 2 to branch 4, so, in general, $q(\dot{\nu}_{\mathrm{MW}}) \sim p(2|3)(1 - Q(\dot{\nu}_{\mathrm{MW}})$. Note that a transition between branches 2 and 4 does not generate net polarization and must satisfy the condition $p(2|4) \equiv p(1|3)$. In addition, the correction ensures that the sum of all populations before and after the crossing remains unchanged. Finally, the factor $g(\dot{\nu}_{\mathrm{MW}}) \sim 1 - \exp(\dot{\nu}_{\mathrm{MW}}/k)$ accounts for the cumulative effect of a varying number of sweeps within a fixed measurement time at a given sweep rate, and k is a parameter gauging the impact of spin diffusion. A more detailed discussion on this last point is addressed in Section IV.

III. Statistical sampling

In the cases where averaging over configurations is required (e.g., Figs. 3, 4A, 5), we perform a simultaneous sampling over angular coordinates (θ, ϕ) and the hyperfine interaction. In particular, we recall that the variables (θ, ϕ) correspond to the direction of the external magnetic field in the crystal-frame where the z-direction is given by the NV crystalline field. Thus, we use the standard homogeneous spherical distribution,

$$\theta = \cos^{-1}(2r_1 - 1)$$

$$\phi = 2\pi r_2$$

where r_1, r_2 are uniform pseudorandom numbers in the interval $(0,1)$.

The hyperfine tensor is assumed to have the following structure:

$$\mathbf{A} = \begin{bmatrix} A_{\mathrm{xx}} & 0 & A_{\mathrm{zx}} \\ 0 & A_{\mathrm{yy}} & 0 \\ A_{\mathrm{xz}} & 0 & A_{\mathrm{zz}} \end{bmatrix}, \tag{A.34}$$

with $A_{\mathrm{xx}} = A_{\mathrm{yy}} = s_1 a$, $A_{\mathrm{zz}} = s_2 a$, and $A_{\mathrm{xz}} = A_{\mathrm{zx}} = 0.3a$. Here s_1, s_2 are pseudorandom binary variables that account for sign randomization (they can be either +1 or -1). For each realization, the value of a is taken from a uniform distribution in the interval $(0, \|A\|_{max})$. As an example, we show in Fig. S3 the simulated ^{13}C NMR signal obtained for different values of $\|A\|_{max}$.

Since the best agreement with the experimental results is achieved when $\|A\|_{max} < 1$ MHz, it is natural to ask if the interaction can be strictly dipolar. In fact, we have verified that nearly identical results can be obtained by using in our simulations the standard dipole-dipole interaction instead of the generic tensor in Eq. (A.34).

IV. Numerical simulation

In order to reconstruct the ^{13}C NMR signal as in Figs. 3, 4A, and 5, we compute the explicit time dependence of each MW sweep. More specifically, the time of each sweep is $\tau_{\mathrm{s}} = \Delta\nu/\dot{\nu}_{\mathrm{MW}}$, where $\Delta\nu$ is the frequency window of the sweep and $\dot{\nu}_{\mathrm{MW}}$ the sweep velocity. We divide the frequency window in steps of $\delta\nu = 100$ Hz and evaluate stepwise the time evolution at each of these frequencies by exact diagonalization of the effective Hamiltonian H_{eff} (Eq. (4) in the main text). The time t_{bin} spent at each frequency bin is given by the ratio between the time of the sweep and the number of bins, i.e. $t_{\mathrm{bin}} = \tau_s/(\Delta\nu/\delta\nu)$. The final state of each bin is used as the initial state for the following bin.

At the beginning of any sweep, we assume that the initial state of the NV is given by

$$\rho_i^{\mathrm{NV}} = \tfrac{(1+\varepsilon)}{3}|0\rangle\langle 0| + \tfrac{(1-\varepsilon/2)}{3}(|-1\rangle\langle -1| + |+1\rangle\langle +1|)\,, \tag{A.35}$$

where the parameter ε controls the NV polarization generated by light-induced spin initialization. In practice, this means that we deterministically project the NV state into ρ_i^{NV}. This projection accounts for the repolarization of the NV while keeping the ^{13}C spin state unchanged. We emphasize that when the sweep is broad enough to encompass both the $m_{\mathrm{S}} = 0 \leftrightarrow m_{\mathrm{S}} = -1$ and $m_{\mathrm{S}} = 0 \leftrightarrow m_{\mathrm{S}} = +1$ sets of transitions, we assume the light intensity is sufficient to repolarize the NV in the time spent sweeping the MW frequency from one set to the next. The same repolarization is assumed to happen in the case of consecutive sweeps of the same subset. Moreover, in all simulations we assume that the NV repolarizes to the same level (defined by the parameter ε) irrespective of the sweep velocity. This is in fact a crude approximation, since for very high velocities there is only a very short time between successive sweeps (or between the two manifolds) and therefore the NV repolarization is less efficient. As we stated in the main text, the NMR signal enhancement is expected to be optimal when the time separation between successive sweeps is brought to a minimum defined by the NV repolarization time. We discuss the case of an unpolarized NV in Section V.

For given angular coordinates (θ, ϕ), it is crucial to know the exact location of each resonance (i.e. LZ crossings) in the frequency space. This is particularly important in reproducing the actual shape (MW frequency dependence) of the experimental NMR signal. So, even though the dynamics of polarization is evaluated in the rotating frame by means of H_{eff}, the actual location of each signal contribution in the frequency axis is determined by diagonalizing the exact Hamiltonian without MW irradiation (i.e. Eq. A.1). This reshuffling procedure allows for the correct distribution of the LZ processes along the frequency domain.

The appropriate quantification of spin diffusion is relevant when reconstructing the NMR signal after multiple sweeps with a fixed total time T. In such case, it is relevant to compare the time τ_{s} between two successive sweeps with the time τ_{d} at which the polarization diffuses away from the ^{13}C directly coupled to the NV. On the one hand, in the limit of low velocities $\dot{\nu}_{\mathrm{MW}} \to 0$, we have $\tau_{\mathrm{s}} \gg \tau_{\mathrm{d}}$, so the generated nuclear spin polarization scales linearly with the number of sweeps $n = T/\tau_{\mathrm{s}}$. In the opposite limit of high velocities $\dot{\nu}_{\mathrm{MW}} \to \infty$, many sweeps take place until the polarization diffuses away from the directly coupled ^{13}C. In this latter case, the total polarization is dominated by the efficiency of the transfer between the NV and the ^{13}C. For any intermediate case, a given number of sweeps is performed until the polarization can actually diffuse away and build up the 'bulk' polarization. We show in Fig. S4 a flow chart that explains the algorithm used in our simulation.

Given the complexity of the many-body problem and the energy mismatch between the ^{13}C coupled and the rest of the 'bulk' carbons, it is hard to have a fair estimate for τ_{d}. A lower bound is given by the spin-spin interaction time T_2, which for ^{13}C in naturally enriched samples is $\sim$10 ms. However, the actual diffusion process can be much slower than that, with estimated scale as long as $\sim 50 \times T_2$ (3).

Due to the uncertainty in some of the parameters (effective laser power, NV spin-lattice relaxation time and level of spin polarization, effective nuclear spin diffusion time, etc.), a comparison between the calculated ^{13}C spin polarization in our NV–^{13}C model upon a single sweep (~5%, see Figs. 4C, 5A, 5C) and the measured *bulk* carbon polarization (of order 0.1%) is difficult. We can, nonetheless, attain a crude estimate when we note that for a sample with natural ^{13}C content (~1%) and 1 ppm NV concentration, there are approximately 10^4 carbons per NV. For the optimal conditions of sweep velocity, it takes ~10 ms to complete one full sweep; therefore, assuming a spin diffusion time of 100 ms, a total of 10 sweeps can bring the polarization of a single carbon on par with that of the NV (~10% for our present experimental conditions). During a 10 s illumination, that corresponds to polarizing 100 carbons to about 10 percent, or 10 fully polarized carbons per NV. Out of the 10^4 carbons, that corresponds to a bulk ^{13}C spin polarization of 0.1%, comparable to the measured values.

V. Light-induced stochastic jumps and the ratchet effect

Other than the deterministic projection into state (A.35), an alternative, more realistic way to introduce light-induced NV repolarization makes use of stochastic quantum jumps (4). Here, one can assume that an initially unpolarized NV undergoes an instantaneous repolarization event with some unit time probability p_{r}, in turn, dependent on the light intensity. In such an event or 'jump', the state of the NV collapses into $|0\rangle\langle 0|$. The actual ^{13}C spin polarization emerges as the result of an average over a sufficiently large number of stories or trajectories.

In order to illustrate the usefulness of the 'jump' approach, we show in Fig. S5 a sequence of three consecutive sweeps. During sweep one, the NV state is polarized by a first jump at a time when the MW frequency is approximately 2.750 GHz, and nuclear spin polarization emerges upon traversing the LZ crossings (see Figs. S5A through S5C). During sweep two (Figs. S5D through S5F), no early NV spin repolarization occurs and traversing the LZ avoided crossings leads to nuclear *depolarization*. A subsequent jump event repolarizes the NV and the third sweep is able to create net polarization again (Figs. S5G through S5I). This example clearly shows that even when rare events of no-repolarization before sweeping happen (and degrade the signal), the system recovers immediately after the next NV spin repolarization. In this sense, the MW sweep in the presence of light acts as a nuclear spin polarization ratchet.

The jump picture is also useful to show the relative fragility of nuclear spin polarization induced via strong hyperfine interactions. Assuming near optimal sweep rate, no polarization can be created if the jump event occurs in between two consecutive LZ crossings within the same $m_s = +1$ or $m_s = -1$ manifold as shown in Fig. S6 for the LZ subset $m_s = 0 \leftrightarrow m_s = -1$ and $\|A\| = 10$ MHz. Since this 'fragile' region where the mechanism is sensitive to light is as large as $\mathrm{A_{zz}}$, strongly coupled carbons are comparatively more sensitive to depolarization than those more moderately coupled (i.e. $\|A\| \lesssim 1$ MHz). Note that this observation adds to the trend already highlighted in Fig. 3A of the main text, already favoring moderately coupled carbons in their ability to transfer polarization to the bulk.

The averaging procedure implicit in the use of the quantum jump picture is independent from (and complementary to) the configurational average described in Section III (where the sampling is carried out over all hyperfine couplings and relative magnetic field orientations). So, even though this approach is physically more accurate, its use is computationally more demanding and thus must be restricted to select cases. Whenever possible, nonetheless, we have verified the equivalence between results obtained using the quantum jump picture and the deterministic initialization of the NV spin.

---

1. Ernst RR, Bodenhausen G, Wokaun A (1987) *Principles of Nuclear Magnetic Resonance in One and Two Dimensions* (Clarendon Press, Oxford).
2. Waugh JS (2007) Average Hamiltonian Theory. *Encycl. Magn. Reson.* (John Wiley and Sons, Ltd.).
3. Reynhardt EC, High GL (1998) Dynamic nuclear polarization of diamond. I. Solid state and thermal mixing effects. *J. Chem. Phys*. 109(10):4090-4099.
4. Plenio MB, Knight PL (1998) The quantum-jump approach to dissipative dynamics in quantum optics. *Rev. Mod. Phys.* **70**(1):101-144.

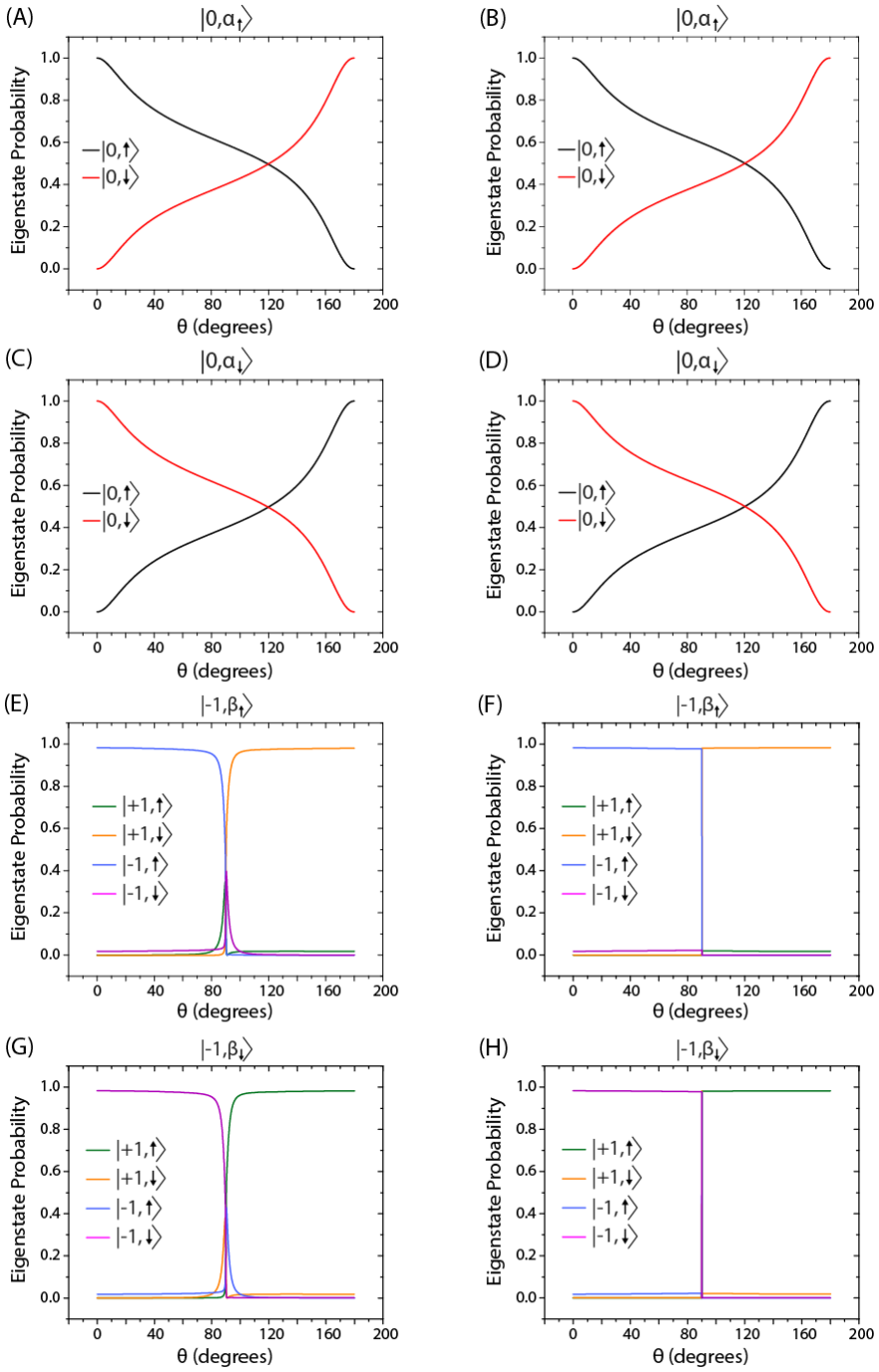

Figure S1. Comparison between the exact Hamiltonian H in (A.1) and the secular approximation $H_{\text{sec}} = H_{\Delta} + \overline{H}^{(0)} + \overline{H}^{(1)}$. In (A), (C), (E) and (G) we plot the decomposition of the exact eigenstates $|0, \alpha_{\uparrow}\rangle$, $|0, \alpha_{\downarrow}\rangle$, $|-1, \beta_{\uparrow}\rangle$ and $|-1, \beta_{\downarrow}\rangle$ respectively in terms of the computational basis states. We do the same in (B), (D), (F) and (G), but using the eigenstates of H_{sec}. In all cases, $\phi = 0$, $A_{\text{xx}} = A_{\text{yy}} = A_{\text{zz}} = 1$ MHz, $A_{\text{xz}} = 0.3A_{zz}$ and $B = 10$ mT.

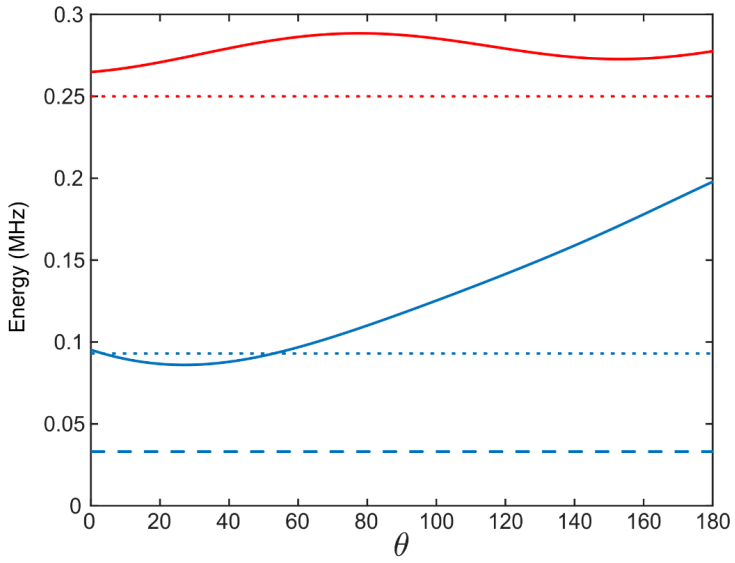

Figure S2. Calculated energy gaps δE_{13} and δE_{23} as a function of θ, for $\phi = 0$ (solid red and blue traces, respectively). The resonance condition corresponds to the transition $|0,\downarrow\rangle \leftrightarrow |-1,\uparrow\rangle$. The choice of parameters is: $A_{\mathrm{zz}} = A_{\mathrm{xx}} = A_{\mathrm{yy}} = 750$ kHz, $A_{\mathrm{zx}} = 0.3A_{\mathrm{zz}}$, $|\vec{\boldsymbol{B}}| = 10$ mT, $\Omega = 250$ kHz. The dashed, blue trace corresponds to the "virtual" gap $2J_{virtual} = \Omega A_{\mathrm{zx}}/2(\omega_{0I} + A_{\mathrm{zz}})$ and the dotted, blue trace corresponds to Eq. (A.26). The dotted, red trace corresponds to the estimate $\delta E_{13} \sim \Omega$.

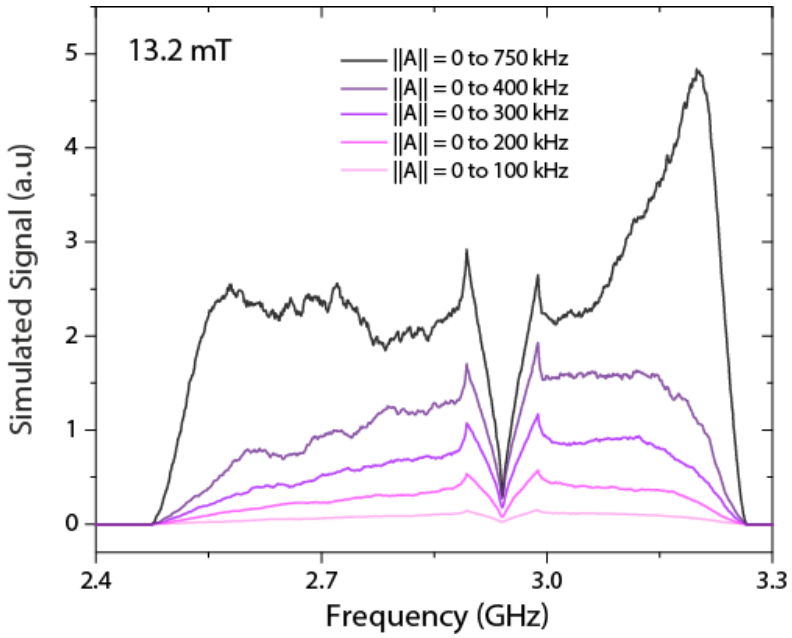

Figure S3. Simulated ^{13}C NMR signal for a 50-MHz-wide MW frequency sweep centered at a variable central frequency. Here, we assume the external magnetic field is $B = 13.2$ mT and consider 1.5×10^4 configurations for (θ, ϕ) and the hyperfine interaction, whose magnitude is taken from the uniform distribution $[0, \|A\|_{max}]$.

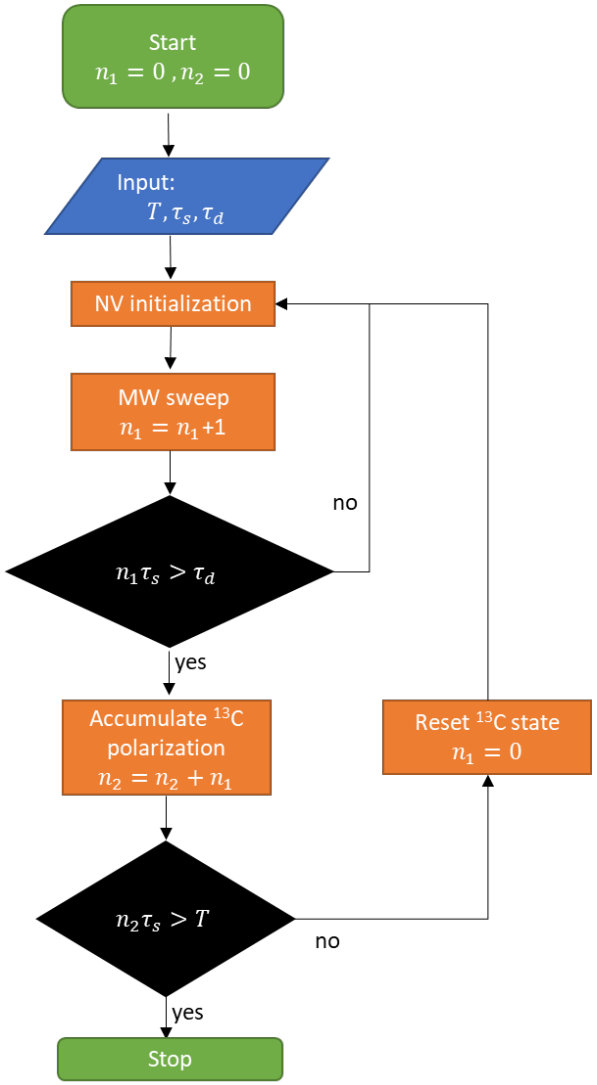

Figure S4. Flow chart for simulating the effect of diffusion in a multiple-sweep, fixed-time protocol. The input variables are the total time T (typically 1 sec), the time per sweep $\tau_s = \Delta\nu/\dot{\nu}_{MW}$ and the diffusion time τ_d. The index n_1 controls the number of sweeps until a 'diffusion event' takes place. In such a case, the nuclear magnetization is accumulated and the state of the system (NV-^{13}C pair) is reset. The algorithm stops after a total time T has elapsed, which means that the index n_2 equals $n = T/\tau_s$.

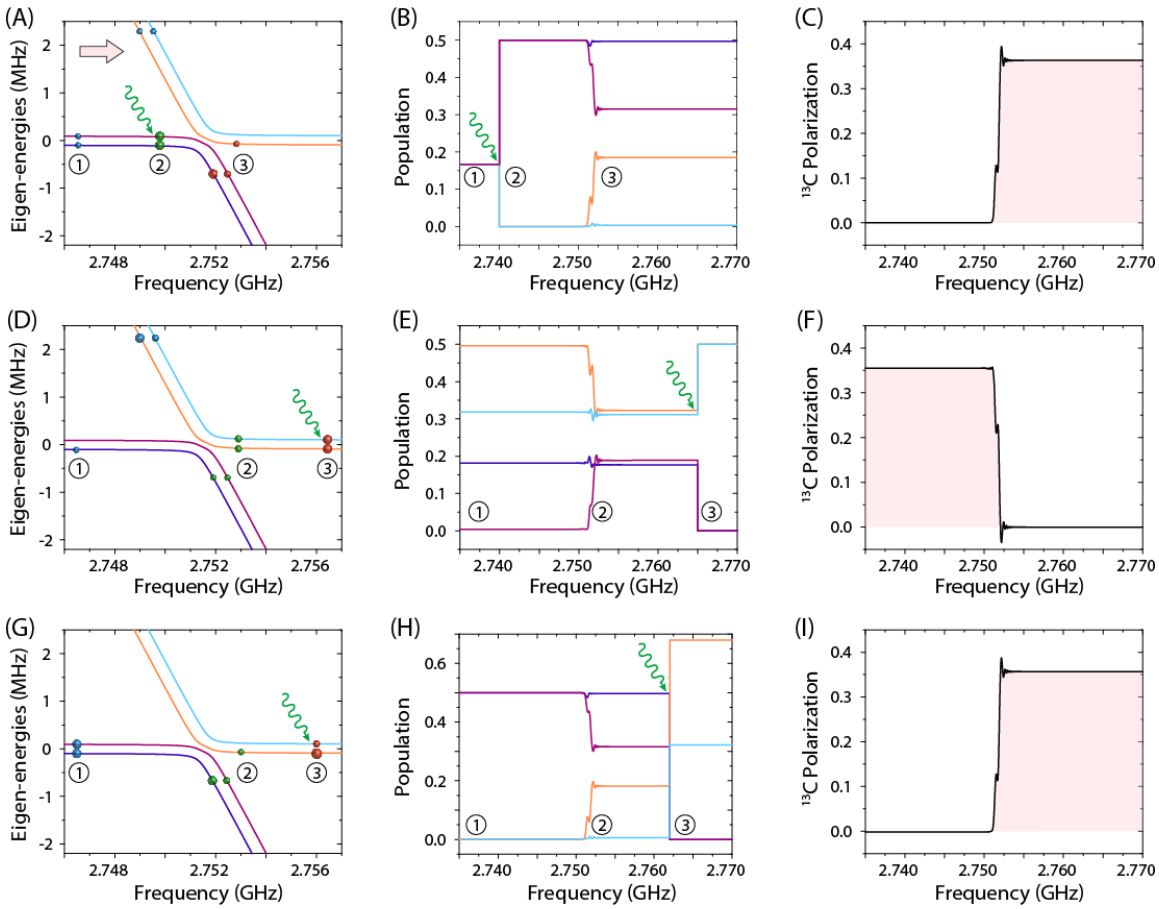

Figure S5. Multiple sweeps in the presence of light-induced stochastic jumps. For the present example, $\theta = 65°$, $\phi = 0°$, and $A_{xx} = A_{yy} = A_{zz} = 500$ kHz, and $A_{xz} = 0.3A_{zz}$. In (A), (D), and (G) the labels for states at each energy curve are the same as in Fig. 2A in the main text. Blue circles indicate initial state ①, green circles indicate the intermediate state ②, and red circles denote the final state ③. A wiggly green arrow indicates a light-induced repolarization event or jump. In (A), we start with a completely unpolarized initial state ①, which subsequently collapses into the subspace $m_s = 0$ upon NV spin optical pumping (state ②); nuclear spin polarization emerges after a MW sweep across the LZ crossing (state ③). In (B) we explicitly show the evolution of these populations and in (C) the corresponding ^{13}C polarization. In (D-F) we show evolution during the second sweep assuming the initial state ① (blue circles in (D)). After the LZ crossing the polarization is lost (state ②, green circles) since there is no more nuclear spin population imbalance. An NV spin repolarization jump in ③ brings back the NV population to the subspace $m_s = 0$ (with no effect on the ^{13}C polarization). In (G-I) we show that under these conditions the third sweep creates again ^{13}C polarization (state ②) and a final NV spin repolarization (state ③) brings the system population to the subspace $m_s = 0$. In this case, a fourth sweep would add more ^{13}C polarization instead of destroying it.

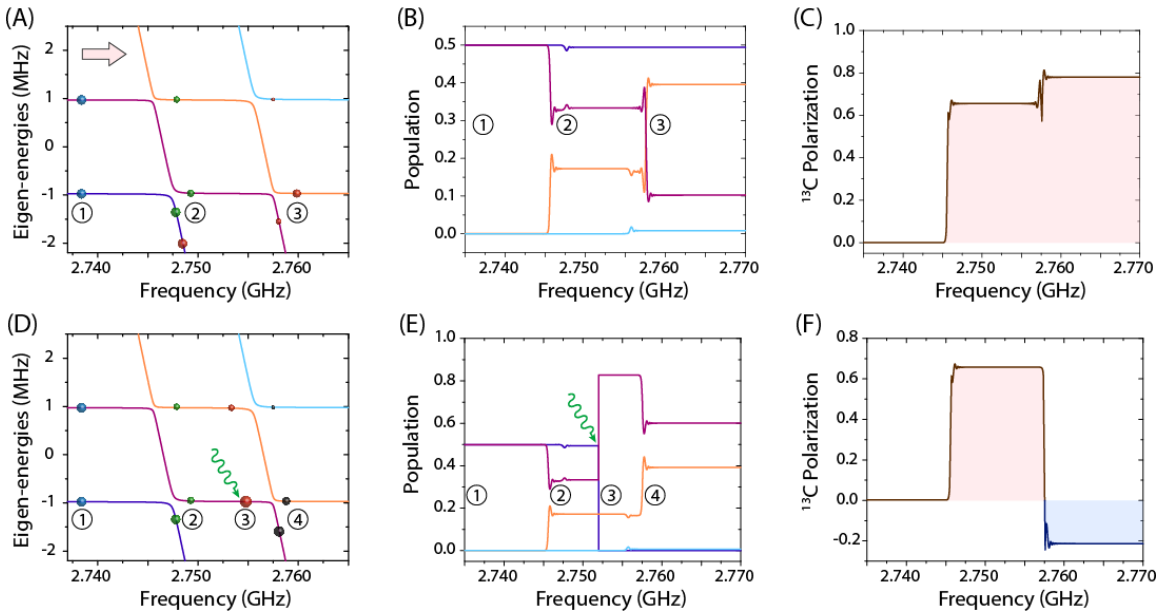

Figure S6. Single MW sweeps for large hyperfine in the presence of light-induced stochastic jumps. In this example, $\theta = 65°$, $\phi = 0°$, and $A_{xx} = A_{yy} = A_{zz} = 10$ MHz, and $A_{xz} = 0.3A_{zz}$. In (A) and (D) the labels for states in each energy curve are the same as in Fig. 2B in the main text. In (A-C) we show a single sweep for an initially polarized NV (blue circles, state ①). The first LZ crossing already generates ^{13}C polarization (green circles, state ②). The second LZ crossing generates even more nuclear spin imbalance (red circles, state ③). In (D-E) we repeat the same simulation but with a jump at a time between the two LZ crossings. This NV spin repolarization event brings the population in $|-1, \beta_\uparrow\rangle$ back into the state $|0, \alpha_\uparrow\rangle$ (red circles in (D), state ③). The second LZ crossing not only destroys the net ^{13}C polarization created, but it turns it into negative (black circles, state ④).